Application of Fe–Cr alloys to solid oxide fuel cells for cost-reduction Oxidation behavior of alloys in methane fuel

Teruhisa Horita*, Yueping Xiong, Haruo Kishimoto, Katsuhiko Yamaji,
Natsuko Sakai, Harumi Yokokawa

*National Institute of Advanced Industrial Science and Technology (AIST), AIST Tsukuba Central 5,
Higashi 1-1-1, Tsukuba, Ibaraki 305-8565, Japan*

Abstract

Oxide scale formations in anode gas atmospheres were investigated for three different Fe–Cr alloys as interconnects in solid oxide fuel cells (ZMG232, SUS430, and Fe–Cr–W). Oxidation with anode gases (CH_4, H_2O, CO, and CO_2) caused a relatively thick oxide scale formation on the alloy surfaces even in low oxygen partial pressures at 1073 K. The distribution of elements in the oxide scale and the growth rates of oxide scales were compared among the examined alloys by glow discharge optical emission spectrometry (GDOES). Mn–Fe–Cr spinels and Cr_2O_3 were formed on ZMG232 and SUS430 surfaces, whereas only Cr_2O_3 formation was observed on Fe–Cr–W surface. Oxide scale thickness grew with annealing time by a parabolic relationship, and the growth rates were in the orders of 10^{-6} to 10^{-5} $\mu m^2 s^{-1}$ at 1073 K. The electrical conductivity after forming oxide scales was different depending on the oxide scale phases and thickness. The conductivity was in the order of $10 \, S \, cm^{-2}$ at 973 K for ZMG232 alloy.
© 2004 Elsevier B.V. All rights reserved.

Keywords: SOFCs; Fe–Cr alloy; Oxidation; Anode gases; GDOES

1. Introduction

Recently, many attempts have been made to reduce the operation temperature of solid oxide fuel cells (SOFCs) from 1273 to 1073 K or lower. One advantage of reducing the operation temperature is the application of alloy materials as interconnects, which are expected to provide cost-reduction. Among the candidate alloys, Fe–Cr alloys have attracted much attention for medium operation temperature SOFCs, because of their reasonable price and high mechanical strength [1–15]. However, at operation temperatures, oxide scales are always formed on the alloy surface by the reaction with atmospheric gases. The formation of an insulating oxide layer is not favorable, but is needed in order to provide a stable protective layer. To improve the electrical conductivity in the oxide scales, several elements have been added into the Fe–Cr alloys to form Cr_2O_3-based conductive oxide layers. Hence, it is important to control and analyze the elemental distribution for optimizing the chemical stability and compatibility of scales.

In an O_2 atmosphere, the oxide scale formation and its chemical stability have been examined by many authors [1–10]. On the other hand, in anode gas atmospheres, few authors have reported the oxidation of Fe–Cr alloys and some unclear points have been left regarding the oxidation [10–15]. In anode atmospheres, methane (CH_4) and steam (H_2O) can contact alloys under the internal steam reforming reactions. Also, the reformat gases, such as CO and CO_2 can contact alloys directly. Therefore, these gases can affect the formation mechanism of oxide scales and the stability of oxide scales. In a previous study, we have reported the oxide scale formation on Fe–Cr alloys in $H_2–H_2O$ and in $CH_4–H_2O$ atmospheres [16–18]. The minor elements' distribution was clarified by SIMS techniques. However, the effects of minor additives on the growth of oxide scale and the electrical conductivity have not yet been clarified. The purpose of the present study is to clarify the oxide scale formation mechanism of three different Fe–Cr alloys in $CH_4–H_2O$ fuel atmospheres. We investigate the effect of minor elements on the growth of oxide scales and the electrical conductivity.

* Corresponding author. Tel.: +81-29-861-4542; fax: +81-29-861-4540.
E-mail address: t.horita@aist.go.jp (T. Horita).

2. Experimental

2.1. Samples

Three different ferritic alloys have been selected as test alloys because they form Cr_2O_3-based oxide scales and have been reported as interconnects of SOFCs [5,6,11,12]. The selected Fe–Cr alloys are abbreviated as follows: ZMG232, SUS430, and Fe–Cr–W. The chemical compositions of these alloys are listed in Table 1. The samples were cut into pieces in the size of about $1 \, cm \times 1 \, cm$, and the surfaces were polished with a diamond paste to obtain a mirror surface (up to $1/4 \, \mu m$ grade).

2.2. Oxidation experiments

The alloys were annealed at 1073 K under CH_4–Ar mixture with a saturation of H_2O. A mixture of CH_4 and Ar was passed through H_2O (at 50 °C) in a flow rate of $50 \, ml \, min^{-1}$. The mixed gases have the following partial pressure of each gas before feeding to the reactor tube: $p(CH_4) = 0.05 \, bar$, $p(Ar) = 0.85 \, bar$ and $p(H_2O) = 0.10 \, bar$. The oxidation treatments were examined at 1073 K for 72–1050 h in an Al_2O_3-tube reactor. When the mixed gases were supplied to the reactor at 1073 K, the CH_4–H_2O gas should be converted to the following composition assuming that equilibrium is attained in the reactor: $p(O_2) = 2.58 \times 10^{-20} \, bar$, $p(H_2) = 1.46 \times 10^{-1} \, bar$, $p(H_2O) = 1.60 \times 10^{-1} \, bar$, $p(CO) = 3.59 \times 10^{-2} \, bar$, $p(CO_2) = 9.56 \times 10^{-3} \, bar$. In this gas composition, the equilibrium calculation suggests no carbon deposition. After the experiments, there was indeed no carbon deposited in the Al_2O_3 reactor tube.

2.3. Analysis of oxidized alloys

Microstructures of cross-sections of oxide scale were analyzed by scanning electron microscope (SEM, Hitachi S-800) with EDX (Kevex). The reaction phases formed on the alloy surface were identified by X-ray diffraction (XRD; Phillips PW 1800). Major and minor elements distributions in depth directions were analyzed by glow discharge optical emission spectrometry (GDOES, Jobin Yvon/HORIBA, JY-5000RF) with Ar sputtering. The depth profiles were measured in an area of 2 mm in diameter. For the RF-generator, the following condition was selected to measure the oxide scales and alloy: pressure, 600 Pa and power, 35 W. After the formation of craters, the depths were analyzed by a surface profiler system (Dektak, Veeco).

The electrical conductivity of oxidized alloys was measured by 4-probe ac impedance measurements [10]. Pt-paste electrodes were applied to the oxidized alloy surfaces, and the measurements were conducted in an air atmosphere. The measurement time for the conductivity was 5 h. The ac impedance spectra were measured in the frequency range from 1 mHz to 100 kHz with amplitude of 10 mV.

3. Results and discussion

3.1. X-ray diffraction of oxidized surfaces

To confirm the reaction products at the oxidized alloy surface, XRD was examined. Fig. 1 shows XRD patterns of oxidized alloys (oxidized at 1073 K for 288 h in CH_4–H_2O). In the XRD pattern of ZMG232 (Fig. 1(a)), the identified peaks are alloy ("A" in figures), Fe–Mn–Cr spinels ("S"), and Cr_2O_3 oxides ("C"). Thus, the oxide scales are mainly composed of spinel and Cr_2O_3 phases. In Fig. 1(b), similar XRD patterns are observed in the oxidized SUS430. In addition to the spinel phases, several peaks attributed to Cr_2O_3 are observed in the pattern, and the intensities are stronger than those of ZMG232. In Fig. 1(c), the XRD pattern mainly shows Cr_2O_3 and alloy, which is different from the above two patterns. Thus, the main phase in the oxide scale is Cr_2O_3 in the case of Fe–Cr–W alloy.

3.2. Microstructures of oxide scale/alloy interfaces

Fig. 2 shows scanning electron microscope images around the oxide scale/alloy interfaces after annealing at 1073 K for 1050 h in CH_4–H_2O. The microstructures of oxide scales show relatively thick and dense layers on the alloy surface. The thickness of oxide scale on each alloy is estimated as follows: ZMG232, $4.8 \, \mu m$; SUS430, $6.1 \, \mu m$; and Fe–Cr–W, $14 \, \mu m$. For the ZMG232 (Fig. 2(a)) and SUS430 (Fig. 2(b)) alloys, the microstructures at the oxide scale/alloy interfaces are very clear without any voids and cracks. Thus, the oxide scales grew continuously from the surface by reacting with atmospheric gases, such as H_2O, CO, and CO_2. On the other hand, some voids are observed at the thick oxide scale/alloy interface of Fe–Cr–W alloys (Fig. 2(c)). These voids can be formed during the oxidation or during the polishing treatments. Because the oxide scale formation causes a significant interdiffusion of cations around the interfaces, cation transport may affect change in the microstructures around

Table 1
Chemical compositions of Fe–Cr alloys examined for oxidation analysis

	ZMG232 (Hitachi Metals Ltd., Japan)	SUS430 (purchased from Nilaco Co.)	Fe–Cr–W (Sumitomo Special Metals Co. Ltd., Japan)
C	0.02	0.048	–
Si	0.40	0.35	0.31
Mn	0.50	0.21	0
Ni	0.26	0.12	0
Cr	21.97	16.35	19.72
Al	0.21	0.05	0.55
P	0	0.023	0
Zr	0.22	–	0.30
La	0.04	–	0
W	0	0	7.03
Fe	76.38	82.849	72.09

Figures are in mass%.
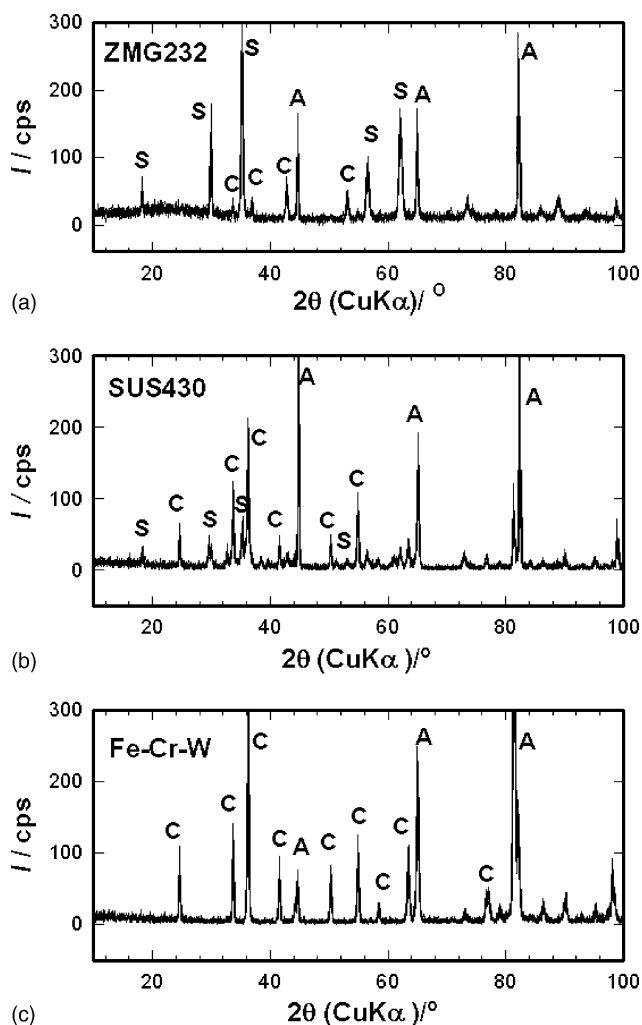
Fig. 1. XRD patterns of oxidized alloys (A: alloy, C: Cr_2O_3, S: spinel, oxidation at 1073 K for 288 h in CH_4–H_2O). (a) ZMG232, (b) SUS430, (c) Fe–Cr–W.

Fig. 2. Scanning electron microscope images of cross-section at the oxide scale/alloy interfaces. (a) ZMG232, (b) SUS430, (c) Fe–Cr–W.

the interfaces. In Fig. 2(a), many dark spots are observed in the ZMG232 alloy. These spots correspond to the A_2O_3 internal oxides, which were confirmed by EDX analysis.

3.3. Elemental distributions around the oxide scale/alloy interfaces

Figs. 3–5 show GDOES depth profiles of elements around the oxide scale/alloy interfaces after oxidation experiments at 1073 K for 144 h. The *x*-axis of these profiles is the depth from the sample surface, and *y*-axis indicates the optical emission intensities of each element. The depth of the crater is measured by a surface profiler system (Dektak, Veeco). In the depth profiles of ZMG232 alloy (Fig. 3), the thickness of the oxide scale is estimated to be about 1.5 μm because of the constant intensities of O in the depth range of 0–1.5 μm. Around the oxide scale/alloy interfaces, the following zones are identified from the surface to the inner oxides: a high concentration zone of Mn and Fe (Mn–Fe
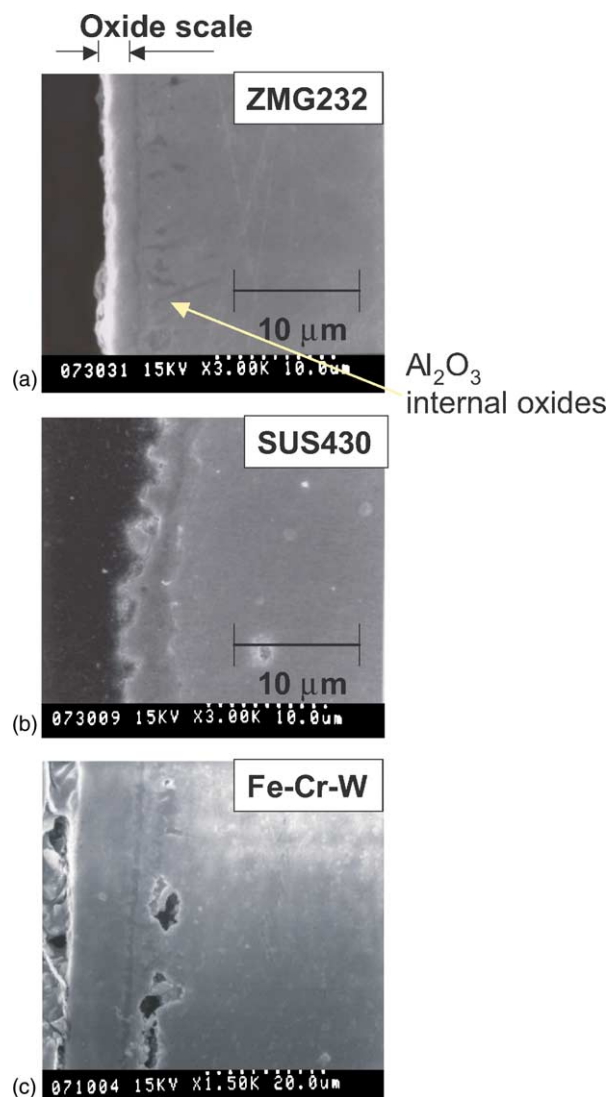
spinels), a Cr-rich zone (Cr_2O_3), and a Si-rich zone. In the SUS430 alloy (Fig. 4), the distribution of elements is similar to that of ZMG232. The oxide phases identified are the following, from the surface to the inner oxides: an Fe–Mn rich phase, a Cr-rich zone, and a Si-rich zone. The minor difference between ZMG232 and SUS430 is the distribution of Al. Since ZMG232 alloy contains much Al, the Al_2O_3 internal oxides were formed in the alloy bulk, as were observed in dark spots in Fig. 2(a). The Mn–Fe–Cr rich zone is identified as a spinel-type structure by XRD analysis of oxidized ZMG232 and SUS430 surfaces (Fig. 1). In the depth profile of Fe–Cr–W (Fig. 5), the following zones are observed from the surface to the inner oxide: a Cr-rich zone and a Si-rich zone. A relatively thick Cr_2O_3 oxide layer was formed (about 5 μm) on the alloy surface compared with ZMG232 and SUS430. The distribution of W was not observed because the instrument did not have a photo multi-meter at the corresponding wavelength.
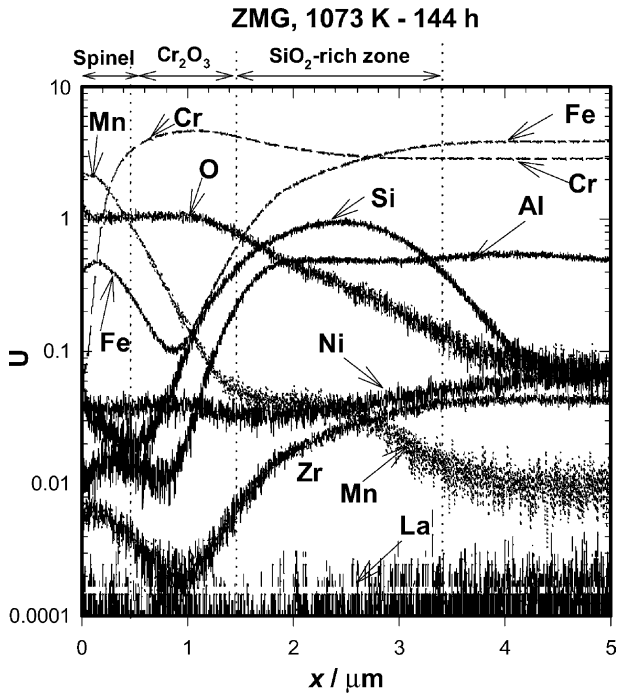
Fig. 3. GDOES depth profile for each element around the oxide scale/alloy interfaces (ZMG232 alloy, oxidation at 1073 K for 144 h).

No spinel phases were identified from the distribution of cations and XRD analysis. The growth rate of oxide scale in Fe–Cr–W alloy is considered to be very high compared with that in ZMG232 and SUS430. From the GDOES depth profiles for the three different alloys examined, the distribution of Si seems to be most important for the formation
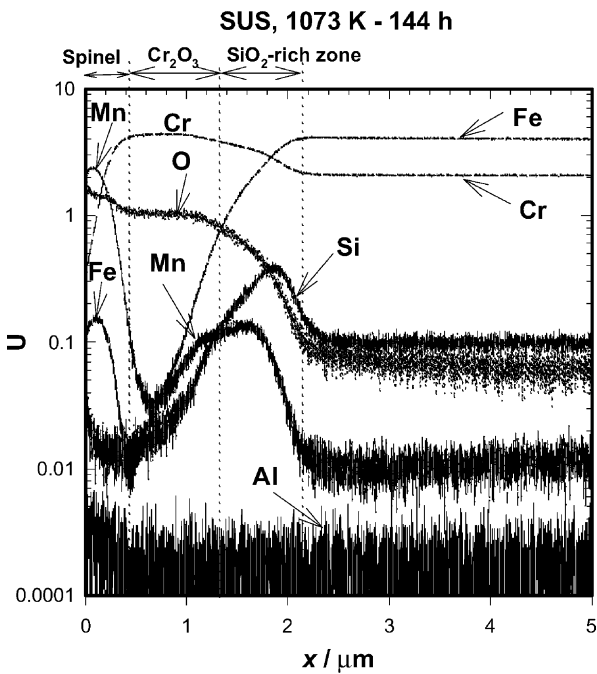

Fig. 4. GDOES depth profile for each element around the oxide scale/alloy interfaces (SUS430 alloy, oxidation at 1073 K for 144 h).
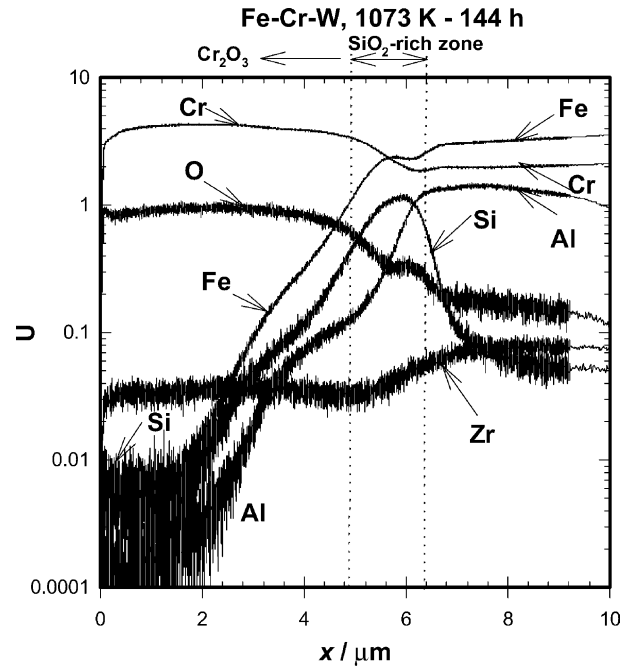

Fig. 5. GDOES depth profile for each element around the oxide scale/alloy interfaces (Fe–Cr–W alloy, oxidation at 1073 K for 144 h).

of conductive stable oxide scale/alloy interfaces. Since Si is condensed at the oxide scale/alloy for all the examined alloys, the distribution of Si may affect the conductivity of oxide scales and the growth of oxide scale.

3.4. Oxide scale growth kinetics

From the GDOES depth profiles, we can estimate the thickness of oxide scales for each alloy at different duration times. The thickness of the oxide scale was estimated from the flat parts of the oxygen (O) depth profiles. Fig. 6 shows oxide scale thickness as a function of annealing time. The thickness of oxide scale follows the parabolic relationship:

$$x^2 = k_p t \tag{1}$$

where x indicates the thickness of the oxide scale, k_p is the growth rate constant, and t is the annealing reaction time. In Fig. 6, the least square fitting lines are also shown. A relatively good agreement is observed between observed and fitted data. This suggests that the growth of oxide scale is controlled by a diffusion process, such as cation diffusion in the alloy. From the slopes of these fitting lines, we can estimate the growth rates, k_p for each alloy. The calculated values of k_p are as follows: $6.2 \times 10^{-6}\ \mu m^2\ s^{-1}$ for ZMG232, $1.0 \times 10^{-5}\ \mu m^2\ s^{-1}$ for SUS430, and $6.5 \times 10^{-5}\ \mu m^2\ s^{-1}$ for Fe–Cr–W. The growth rates of ZMG232 and SUS430 are similar in the orders of magnitude. On the other hand, the growth rate of oxide scale in the Fe–Cr–W alloy is considerably high. The growth rate of oxide scale can be controlled by the addition of minor elements, such as Si, Al, Mn, La, and Zr. Addition of Mn and La can be effective to reduce the
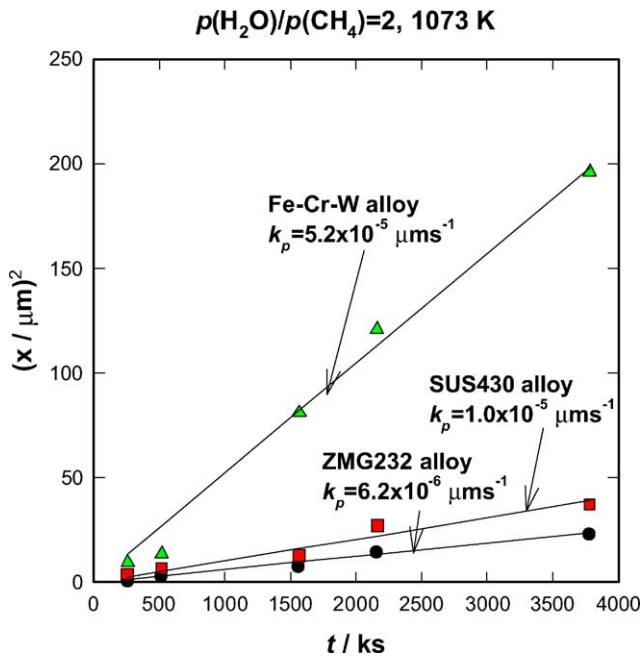
Fig. 6. Oxide scale thickness as a function of annealing times for three different alloys (●: ZMG232, ■ : SUS430, ▲ : Fe–Cr–W).

oxide scale growth rates by forming the Mn–Fe–Cr spinel phases on the surface. From these oxide scale growth rates, we can estimate the thickness of oxide scale for a long-term operation. In ZMG232 alloy, the thickness of oxide scale will be about 14 and 30 μm for 1 and 5 years' operation, respectively.

3.5. Electrical conductivity of oxidized alloys

The electrical conductivity after forming the oxide scale was measured by 4-probe methods. An area specific resistance (R_{AS}) was adopted to evaluate the resistance of the samples:

$$R_{AS} \, (\Omega \, cm^2) = RS \tag{2}$$

where R and S indicate the measured resistance and the surface area of the samples, respectively. The R_{AS} can contain the resistance from oxide scales and alloy bulk. Since we cannot measure the exact effective oxide thickness of scales, we adopted the R_{AS} as a resistance of the oxidized alloy. Fig. 7 shows electrical conductivity ($\sigma = R_{AS}^{-1}$) as a function of inverse temperature. The electrical conductivity increases with increasing temperatures, which is semiconductor temperature dependence. Thus, the electrical conductivity can indicate the contribution from the oxide scales formed on the Fe–Cr alloys. The electrical conductivity of ZMG232 shows higher values than the other alloys (area specific resistance, $R_{AS} \approx 0.1$–$0.2 \, \Omega \, cm^2$ at 973 K). High electrical conductivity can come from a relatively thin oxide scale and spinel (Mn–Fe–Cr) formation on the surface. The difference in the electrical conductivity between ZMG232 and SUS430 can come from the oxide scale thickness and microstructures.
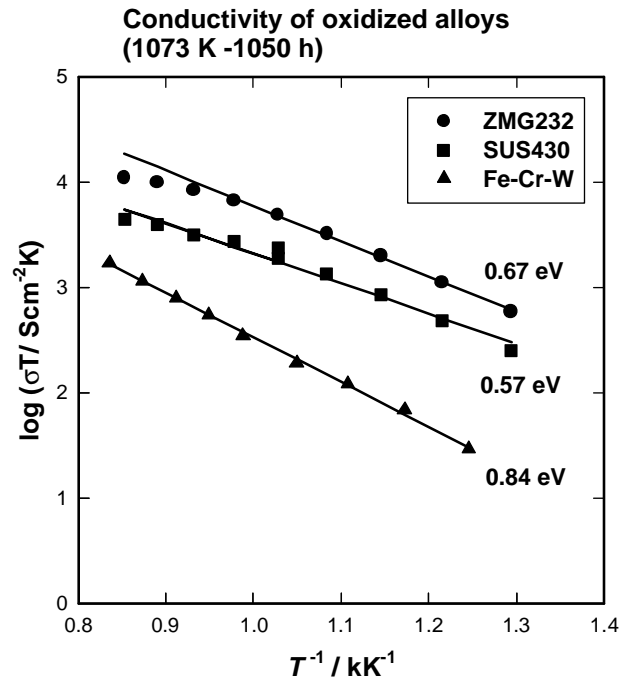

Fig. 7. Electrical conductivity of oxidized alloys as a function of inverse of temperature (oxidation at 1073 K for 1050 h, ●: ZMG232, ■: SUS430, ▲: Fe–Cr–W).

Relatively low electrical conductivity in the Fe–Cr–W alloy is due to a thick oxide scale and pores formed at the oxide scale/alloy interfaces.

The slope of the $\sigma T (= R_{AS}^{-1} T)$ versus inverse temperatures was calculated from the following relationship:

$$\sigma T = R_{AS}^{-1} T = A \exp \left(\frac{-E_a}{kT} \right) \tag{3}$$

where A is pre-exponential constant, E_a is activation energy, k is Boltzman constant, and T is temperature. The activation energy for each oxidized alloy was calculated from least square fitting of the observed data in the temperature range from 689 to 1081 K. The obtained values are 0.67 eV for ZMG232, 0.57 eV for SUS430, and 0.84 eV for Fe–Cr–W alloys. These values are similar to the reported activation energy for the oxidized Fe–Cr alloys [10]. However, they are very high compared to the electrical conduction of Cr_2O_3 (≈ 0.18–0.3 eV). The temperature dependence of the electrical conductivity is affected by the Mn–Fe–Cr spinel phases.

3.6. Possibility and improvements of Fe–Cr alloys as SOFC interconnects

In this study, oxide scale formation was compared among some candidate Fe–Cr alloys in CH_4–H_2O atmospheres. Even in low oxygen partial pressures, oxide scales were formed on the alloy surfaces. Reaction with H_2O, CO, and CO_2 can cause a significant increase in the thickness of oxide scales. The reported growth rates of oxide scales of SUS430 in air ($\approx 10^{-6} \, \mu m^2 \, s^{-1}$) were similar orders of

magnitude with the present data. Thus, the thickness of oxide scale is expected to be similar both in air and in fuel atmospheres for SUS430, which is different from the Ni-based alloys [19,20]. Several minor additions, such as Mn and La, can reduce the oxide scale growth and increase the electrical conductivity in the oxide scales. Thus, the formation of stable and good oxide scales needs these additives to form electrically conductive oxide layers. The Mn–Fe–Cr spinel phase formation seems to be very important to have a conductive oxide layer. In this study, the measured electrical conductivity of oxidized alloys was relatively large (in the orders of $0.1 \, \Omega \, cm^2$ level). In order to improve the electrical conductivity further, coating of the conductive oxide layer such as $LaCrO_3$ on the alloys may be another solution.

In a real SOFC operation, the Fe–Cr alloy interconnects make contact with electrodes ($LaMnO_3$ or $LaCoO_3$ based cathodes and Ni–YSZ cermet anodes). The alloy interconnects may react with the electrodes to form spinel phases at the interconnect/cathode interface [5,6]. Although a high growth rate was observed for oxide scales in the Fe–Cr–W alloy, a relatively stable oxide scale formation was reported with a reaction of a $LaMnO_3$-based electrode [5,6]. The formation of spinel phases can affect the stability of interconnects. The reactivity between Fe–Cr alloy and electrodes is now under investigation, and we will report the stability of interconnects with electrodes in the future.

4. Conclusions

Oxide scale formations were investigated for some candidate Fe–Cr alloy materials (ZMG232, SUS430, and Fe–Cr–W) in CH_4–H_2O atmospheres at 1073 K. Oxidation with anode gases (H_2O, CO, and CO_2) caused a relatively thick oxide scale formation on the alloy surfaces even in low oxygen partial pressures. The distribution of elements in the oxide scale and the growth rates of oxide scales were compared among these alloys. Mn–Fe–Cr spinels and Cr_2O_3 were observed on the ZMG232 and SUS430 surfaces, whereas only Cr_2O_3 formation was observed on the Fe–Cr–W surface. Oxide scale thickness grew with time in a parabolic relationship for all the examined alloys. Growth rates of the oxide scales were in the orders of 10^{-6} to $10^{-5} \, \mu m^2 \, s^{-1}$. The electrical conductivity can be affected by the formation of Mn–Fe–Cr spinels in the oxide scales, which were in the orders of $10 \, S \, cm^{-2}$ at 973 K for ZMG232 alloy.

Acknowledgements

References

[1] W.J. Quadakkers, H. Greiner, M. Hänsel, A. Pattanaik, A.S. Khanna, W. Malléner, Solid State Ionics 91 (1996) 55.
[2] S. Linderoth, P.V. Hendriksen, M. Mogensen, N. Langvad, J. Mater. Sci. 31 (1996) 5077.
[3] Th. Malkow, U.v.d. Crone, A.M. Laptev, T. Koppitz, U. Breuer, W.J. Quadakkers, in: V.U. Stimming, S.C. Singhal, H. Tagawa, W. Lehnert (Eds.), Solid Oxide Fuel Cells, PV97-40, Proceedings Series, The Electrochemical Society Inc., Pennington, NJ, 1997, p. 1244.
[4] S. Lineroth, P.H. Larsen, in: S. Philippe (Ed.), Third European SOFC Forum, 1998, p. 323.
[5] M. Ueda, H. Taimatsu, Mater. Trans. JIM 40 (12) (1999) 1390.
[6] M. Ueda, M. Kadowaki, H. Taimatsu, Mater. Trans. JIM 41 (2) (2000) 317.
[7] K. Honegger, A. Plas, R. Diethelm, W. Glatz, in: S.C. Singhal, H. Yokokawa (Eds.), Solid Oxide Fuel Cells VII, PV2001-16, The Electrochemical Society Inc., Pennington, NJ, 2001, p. 800.
[8] J. Pirmón, Abellán, V. Shemet, F. Tietz, L. Singheiser, W.J. Quadakkers, A. Gil, in: S.C. Singhal, H. Yokokawa (Eds.), Solid Oxide Fuel Cells VII, PV2001-16, The Electrochemical Society Inc., Pennington, NJ, 2001, p. 811.
[9] O. Teller, W.A. Meulenberg, F. Tietz, E. Wessel, W.J. Quadakkers, in: S.C. Singhal, H. Yokokawa (Eds.), Solid Oxide Fuel Cells VII, PV2001-16, The Electrochemical Society Inc., Pennington, NJ, 2001, p. 895.
[10] K. Huang, P.Y. Hou, J.B. Goodenough, Solid State Ionics 129 (2000) 237.
[11] T. Brylewski, M. Nanko, T. Maruyama, K. Przybylski, Solid State Ionics 143 (2001) 131.
[12] T. Uehara, T. Ohno, A. Toji, in: J. Huijsmans (Ed.), Proceedings Fifth European SOFC Forum, European Fuel Cell Forum, 2002, p. 281.
[13] J. Pirón-Abellán, F. Tietz, V. Schemet, A. Gil, T. Ladwein, L. Singheiser, W.J. Quadakkers, in: J. Huijsmans (Ed.), Proceedings of Fifth European SOFC Forum, European Fuel Cell Forum, 2002, p. 248.
[14] T. Uehara, A. Toji, K. Inoue, M. Yamaguchi, T. Ohno, in: S.C. Singhal, M. Dokiya (Eds.), Solid Oxide Fuel Cells VIII, PV2003-07, The Electrochemical Society Inc., Pennington, NJ, 2003, p. 914.
[15] T. Franco, R. Henne, M. Lang, P. Metzger, G. Schiller, P. Szabo, S. Ziehm, in: S.C. Singhal, M. Dokiya (Eds.), Solid Oxide Fuel Cells VIII, PV2003-07, The Electrochemical Society Inc., Pennington, NJ, 2003, p. 923.
[16] T. Horita, Y. Xiong, K. Yamaji, N. Sakai, H. Yokokawa, in: J. Huijsmans (Ed.), Proceedings of Fifth European SOFC Forum, European Fuel Cell Forum, 2002, p. 401.
[17] T. Horita, Y. Xiong, K. Yamaji, N. Sakai, H. Yokokawa, J. Electrochem. Soc. 150 (3) (2003) A243.
[18] T. Horita, Y. Xiong, K. Yamaji, N. Sakai, H. Yokokawa, J. Power Sources 118 (1/2) (2003) 35.
[19] D.M. England, V. Vilkar, J. Electrochem. Soc. 146 (9) (1999) 3196.
[20] D.M. England, V. Vilkar, J. Electrochem. Soc. 148 (4) (2001) A330.